

Compton Scattering

Max Christopher* and Xiaoyuan Zhang†

Department of Physics, Harvard University, Cambridge, MA 02138

We measure the Compton scattering effects from both high energy and low energy sources. The energy shifts with respect to the scattering angle θ completely agree with the Compton shift formula in both cases. Up to a geometry factor, the differential cross section $\frac{d\sigma}{d\cos\theta}$ at high energy also agrees with the Klein-Nishina formula. We also extract the electron momentum distribution function for the aluminum target from the low energy Compton spectrum, which allows further calculations of multiple Compton scattering. Finally, we find a relationship between the atomic mass of the scattering target and the distribution of the energy peak using different targets at a fixed scattering angle.

I. INTRODUCTION

The scattering of photons off of electrons is perhaps one of the most important physical processes in nature. The elastic process is called Thomson scattering [1], as described by classical electromagnetism (EM). Here, the total cross section is constant [2]: $\sigma = (8\pi\alpha^2)/(3m^2)$, where $\alpha \approx 1/137$ is the coupling constant for EM and m is the electron mass. In 1923, Arthur Compton completed the inelastic scattering experiment and found that the outgoing photons lose energy at nonzero scattering angles [3]. This phenomenon is known as the Compton shift, which is described by the relationship

$$\lambda' - \lambda = \frac{h}{mc}(1 - \cos\theta) \quad (1)$$

where λ and λ' are the wavelengths for the incoming photon and outgoing photon respectively. We also have that h is the Planck constant, and θ is the scattering angle. As a quantum effect, Compton scattering plays a very important role in all aspects of physics: from X-ray crystallography to astrophysics. In high energy physics, Compton processes are utilized in the luminosity monitor for the electron-photon collider, and in condensed matter physics, single Compton scattering is the primary building block for Comptonization [4] inside of plasma or other materials.

The theory of Compton scattering has developed with quantum mechanics (QM) and quantum electrodynamics (QED). Early on, Gordon [5] and Dirac [6] developed relativistic QM in order to describe processes like Compton scattering. However, these approaches do not work for spin- $\frac{1}{2}$ fermions. It was not until Dirac proposed his equation for the massive relativistic electron [7] in 1928 that Klein and Nishina managed to calculate the leading order (LO) cross section for Compton scattering $\gamma(p_1) + e^-(p_2) \rightarrow \gamma(p_3) + e^-(p_4)$ [8], given by the Klein-Nishina formula:

$$\frac{d\sigma}{d\cos\theta} = \frac{\pi\alpha^2}{m^2} \left(\frac{\omega'}{\omega}\right)^2 \left(\frac{\omega'}{\omega} + \frac{\omega}{\omega'} - \sin^2\theta\right) \quad (2)$$

where $\omega = 2\pi c/\lambda$ is the angular frequency of incoming photon and similarly, $\omega' = 2\pi c/\lambda'$ for the outgoing photon. In QED, the coupling constant, α , changes with the energy variations due to the loop corrections. However, it is safe to keep $\alpha \approx 1/137$ since the energy range in our experiment is small. We can also integrate Eq. (2) over the phase space and obtain the LO total cross section:

$$\sigma_{LO} = \pi\alpha^2 \left(\frac{2(3m^4 + 6m^2s - s^2) \log\left(\frac{s}{m^2}\right)}{(m^2 - s)^3} + \frac{m^6 - m^4s + 15m^2s^2 + s^3}{s^2(m^2 - s)^2} \right) \quad (3)$$

where s is the Mandelstam variable: $s = (p_1 + p_2)^2$. Notice that in the threshold limit $s \rightarrow m^2$, this equation simplifies to the Thomson scattering limit. The next-to-leading order (NLO) cross section was first considered by Brown and Feynman in 1951 [9] and became available recently [10]. This provides a significant correction at very high energies.

When the energy of the incoming photon becomes comparable to, or less than, the binding energy of the electrons in the materials, the free electron approximation breaks down and we can no longer use the free electron approximation to model the scattering behavior. Since other electrons in the material are not merely spectators, we need to solve the non-relativistic Schrödinger equation under the mean-field approximation in order to obtain the Compton profile $J(p_z)$ [11]:

$$J(p_z) = \iint n(p_x, p_y, p_z) dp_x dp_y \quad (4)$$

where $\vec{p} = (p_x, p_y, p_z)$ is the momentum of the target electron and $n(p_x, p_y, p_z)$ is its probability density distribution. In particular, the frequency shift is captured by the following equation [11]:

$$\lambda' - \lambda = \frac{h}{mc}(1 - \cos\theta) + 2\sqrt{\lambda\lambda'} \frac{p_z}{mc} \sin\frac{\theta}{2} \quad (5)$$

This has the same leading term as Eq. (1), but it has another correctional term dependent upon $\sin(\theta/2)$, which becomes measurable since the electron velocities are surprisingly high near the Fermi surface. At the same time,

* maxwellchristopher@college.harvard.edu

† xiaoyuanzhang@g.harvard.edu

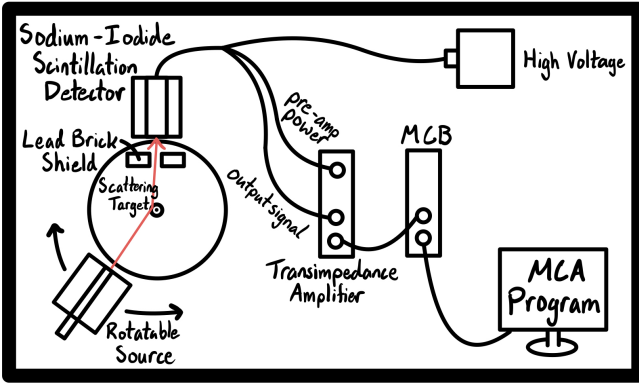


FIG. 1. A diagram of the high energy Compton scattering apparatus, requiring a sodium-iodide detector and lead brick shields.

we can also determine the fully differential electron momentum distribution function (EDF), $f_e(\theta, E_e)$, using the momentum conservation law. Here θ is the scattering angle and E_e is the energy of the outgoing electron. In other words, $f_e(\theta, E_e)$ tells us the probability of finding an electron with energy E_e at the scattering angle θ . The normalization is chosen such that [12]

$$\iint f_e(\theta, E_e) d\theta dE_e = 1 \quad (6)$$

which means the total probability to find an electron is 1. While the EDF usually varies for different targets, it can be applied to multiple Compton scattering processes, like Comptonization [4].

In this experiment, we measure the single Compton scattering from a high energy cesium source and present the Compton shift at different scattering angles. Moreover, we integrate the Compton spectrum over the outgoing photon energy and show that it is in agreement with the Klein-Nishina formula: Eq. (2). We also evaluate a low energy americium source, to show that the energy spectra depends on both the scattering angle and the material of the targets. In particular, we measure the scattering with aluminum and copper targets at different angles to verify the Compton shift correction from Eq. (5). We also extract the electron momentum distribution function from the aluminum target Compton spectrum using momentum conservation and compare the distribution of the energy peaks among different scattering targets.

II. COMPTON SCATTERING EXPERIMENT

A. Compton Scattering Apparatus

To analyze the Compton scattering effect we measured the change in the energy of outgoing photons associated with different scattering angles. The radiation source was

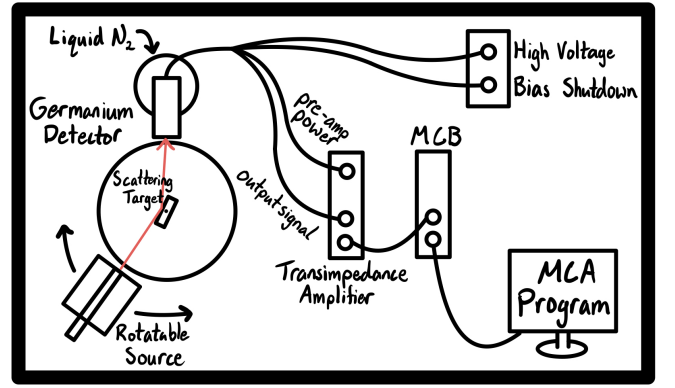


FIG. 2. A diagram of the low energy Compton scattering apparatus, requiring a liquid N₂ cooled germanium detector with a bias shutdown.

placed in a cylindrical lead shield to protect the environment from its radiation. This radiation source was free to rotate about a circular table to change the scattering angle. The scattering target was at the center of the table, and scattered the radiation towards the fixed detector. This allowed us to take energy measurements at precise angular intervals. For these experiments, $\theta = 0^\circ$ is defined to be the angle directly across (180°) from the detector. While this was the basic experiment set-up, we needed to use slightly different equipment for high energy and low energy gamma rays.

The cesium-137 radiation source gave off high energy radiation. This called for a sodium-iodide scintillation detector to be used for energy detection. In order to get the best data resolution, we also had to use a lead brick shield with a 3cm gap in front of the detector (see Appendix 4 for how we determined this gap width). The sodium-iodide detector was powered with high voltage set to 500V. It was also connected to a transimpedance amplifier set to a gain of 200 to increase the signal, with both pre-amp and outgoing signal connections. The signal was then processed by a multichannel buffer (MCB) which could then be read by a multichannel analyzer (MCA) on the computer. The voltage channels were then calibrated as described in Appendix 1. The high energy experiment setup is shown in Fig. 1.

At low energies, the Compton energy shift is relatively small. This required the use of the much more precise germanium detector for our second radiation source of americium-241. As seen in Fig. 2, this experiment has a slightly different apparatus. In this experiment, the germanium detector is mounted in a vacuum chamber which is inserted into a liquid nitrogen (N₂) dewar. The detector must be cooled in order to reduce leakage current, or else the resolution of the device's data would be overwhelmed with noise. To prevent the germanium detector from running without liquid nitrogen cooling, it is plugged into both the high voltage (set to 1500V) and a bias shutdown which turns the detector off if the liquid N₂ runs out and the detector heats up too much.

The rest of the apparatus is identical to the high energy apparatus, but the MCA required its own calibration as described in Appendix 2.

B. Experiment Methods

For our high energy Compton scattering experiment, we used a cesium-137 source with an aluminum target. We then measured the energy spectra of outgoing photons at different angles at ten degree intervals: $\theta = 10^\circ, 20^\circ, \dots, 140^\circ$. The time of measurement was not constant for each angle, as it had to be increased for larger angles in order to achieve an adequate resolution. Therefore, we recorded the time of measurement for each angle and later compared angular spectra using a normalized count rate. We also measured the background spectrum at each angle by simply removing the target and allowing the radiation source to remain. We needed a unique background spectrum for each angle because at different angles we had different (non-scattering) detections of the radiation source. For example, there may have been some direct radiation from the source at low angles and small leakage through the lead shield at large ones. Then we smoothed the background data and subtracted it from the Compton spectrum (see Appendix 3 for details). By identifying the position of the peaks in the spectra by fitting them with a Lorentzian distribution [13, 14], Eq. (20), we could investigate the relationship between the scattering angle and the energy of outgoing photons. Using the Compton shift relation from Eq. (1), we could derive the expected energy shift at some particular scattering angle θ :

$$E' = \frac{1}{\frac{1}{E} + \frac{1}{mc^2}(1 - \cos \theta)} \quad (7)$$

Then, we could plug in the values for the energy of the cesium source (662 keV [15]) and the mass of an electron to find that

$$E' = \frac{1}{0.001511 + 0.001957(1 - \cos \theta)} \text{ (keV)} \quad (8)$$

Then, we could fit the data for high energy scattering with the function $E' = 1/(a + b(1 - \cos \theta))$ and evaluate the accuracy of our experimentally determined values for $a = 1/E$ and $b = 1/(mc^2)$.

We could also calculate the differential cross section with respect to the scattering angle by integrating over the energy. Explicitly,

$$\begin{aligned} \frac{d\sigma}{d\cos \theta} &= \int dE \frac{d\sigma}{dE d\cos \theta} \\ &= \sum_i \Delta E_i \frac{W(E_{i+1}, \theta) - W(E_i, \theta)}{2} \end{aligned} \quad (9)$$

where $W(E_{i+1}, \theta)$ is the experiment data from the energy spectrum, $\Delta E \equiv E_{i+1} - E_i$, and we approximate the integral with the Riemann sum. Since we do not care about

the properties of the cesium source, we can normalize the differential cross section with the normalization factor σ_1 :

$$\sigma_1 = \left. \frac{d\sigma}{d\cos \theta} \right|_{\theta=140^\circ} \quad (11)$$

This allows us to compare $(1/\sigma_1)((d\sigma)/(d\cos \theta))$ with the Klein-Nishina formula. Note that we estimate the error from the counting with Poisson distribution and propagate it to the observables we consider.

To study the low energy Compton spectrum, we used americium-241 as the source, whose radiation energy peak is 59.5 keV [15]. We measured the low energy Compton scattering for both aluminum and copper targets at a variety of different angles. For the aluminum target, we measured the spectrum at ten degree intervals: $\theta = 10^\circ, 20^\circ, \dots, 150^\circ$. Due to much longer measurement times required to get resolved peaks for copper, we measured fewer angles from 40° to 140° . Again, due to different measurement times, we normalized the data to a count rate in order to adequately compare different angles. In both cases, we also measured the background at different angles by removing the target as in the high energy Compton scattering. After subtracting the smoothed background (Appendix 3), we used the Lorentzian distribution to find the peaks of each spectrum. In order to investigate the Compton shift relation at low energies, we needed to fit our data with the correction formula Eq. (5). Thus, we found that the corrected low energy shift became

$$E' = \frac{1}{\frac{1}{E} + \frac{2}{mc^2} \sin^2 \frac{\theta}{2} + \frac{2p_z}{mcE} \sin \frac{\theta}{2}} \quad (12)$$

Then, by plugging in known values, we found that

$$E' = \frac{1}{0.016807 + 0.003914 \sin^2 \frac{\theta}{2} + 0.000066 p_z \sin \frac{\theta}{2}} \text{ (keV)} \quad (13)$$

which depends on the unknown z component of the electron momentum which differs for different targets. However, we can still fit our data for low energy scattering with the function $E' = 1/(a + b \sin^2 \frac{\theta}{2} + c \sin \frac{\theta}{2})$ and compare our values to the theoretical prediction.

At the same time, we can extract the electron momentum distribution function using the momentum conservation law $E'_e = E_\gamma + E_e - E'_\gamma = E_\gamma - E'_\gamma$, since the incoming electron is at rest in the lab frame. In practice, we introduce the dimensionless energy fraction with respect to the source energy $x = E'_e/E_{\text{source}} = E'_e/59.5 \text{ keV}$, and for each scattering angle θ , we first calculate the EDF distribution $\bar{f}(\theta; x)$ directly from the Compton shift. Then we calculate the normalization factor \mathcal{N} :

$$\mathcal{N} = \int_0^1 dx \int_0^{2\pi} d\theta \bar{f}(\theta; x) \quad (14)$$

where the integral is done with the Riemann sum similar to Eq. (10). Eventually we normalize the EDF as

$$f(\theta; x) = \frac{1}{\mathcal{N}} \bar{f}(\theta; x) \quad (15)$$

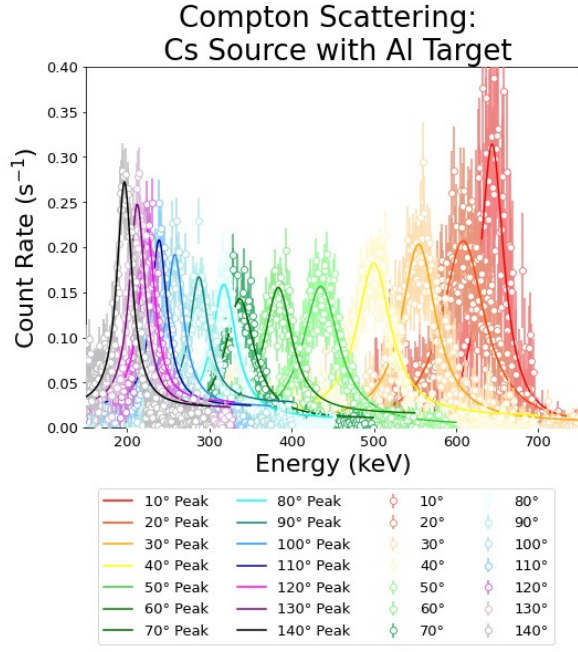


FIG. 3. The high energy Compton shift spectra with an aluminum target.

which satisfies the normalization condition in Eq. (6). For the error estimation, we propagate the error from the count rate (which comes from Poisson distribution), but neglect the error from the energy and the angle.

We also studied the effect of different targets on the Compton shift at fixed angles with carbon, aluminum, vanadium, copper, silver and lead. We measured their energy spectra at $\theta = 80^\circ$, subtracted the smoothed background and fit their distributions with a Lorentzian function. Using the half-width, γ , parameter from the Lorentzian fitting, we were able to investigate the relation between the atomic number of the target and spread of their distributions.

C. The Results of Compton Scattering

The Compton scattering spectra at different angles are shown in Fig. 3. All energy peaks of the outgoing photons are downshifted below the energy of the cesium source. Moreover, the relation between the scattering angle and the peak energy is given in Fig. 4. The curve fitting we get for $E = 1/(a + b(1 - \cos \theta))$ with

$$\begin{aligned} a &= 0.001524 \pm 1.8633 \times 10^{-9} \\ b &= 0.002001 \pm 1.8339 \times 10^{-8} \end{aligned} \quad (16)$$

which is in good agreement with Eq. (8).

The differential cross section distribution is also shown in Fig. 5. Our data strays from the predicted relationship described in Eq. (2) for small angles. There are two main reasons for this discrepancy. First of all, we could

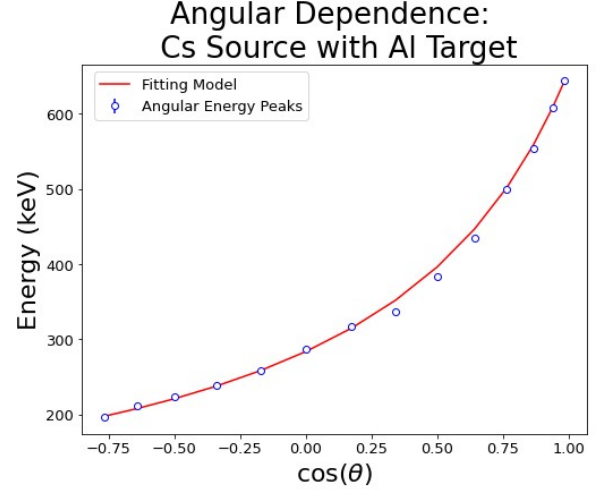


FIG. 4. The high energy Compton shift effect as a function of $\cos(\theta)$, where θ is the scattering angle.

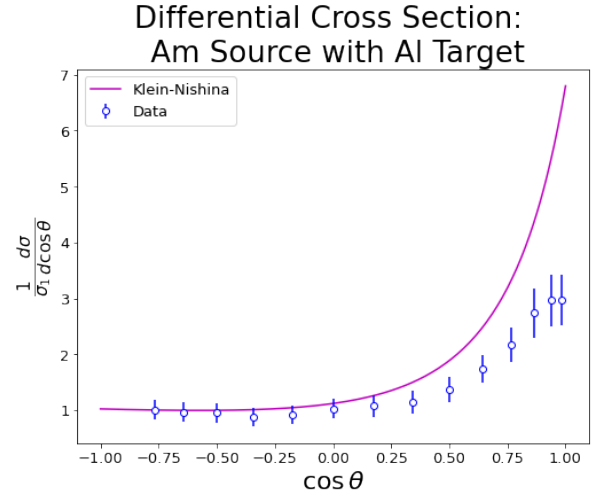


FIG. 5. The differential Compton cross section with respect to $\cos(\theta)$, where θ is the scattering angle.

not obtain the full energy spectrum at each angle due to the detector limits. In other words, the energy cutoff leads to an incomplete contribution, which is less than the prediction of the Klein-Nishina formula. Secondly, since the detector has a finite area, what we were actually measuring in the experiment was

$$W(E_i, \theta) = \int_{\theta-\Delta\theta}^{\theta+\Delta\theta} d\theta \frac{d\sigma}{dE d\cos\theta} \approx \Omega \frac{d\sigma}{dE d\cos\theta} \quad (17)$$

So the normalization constant σ_1 that we used to divide the experimental data has a additional factor Ω , which causes the deviation between the Klein-Nishina prediction and the data. Since this factor Ω relies on the shape of the target and how it reflects the photons, it is too complicated to compute it from geometry directly.

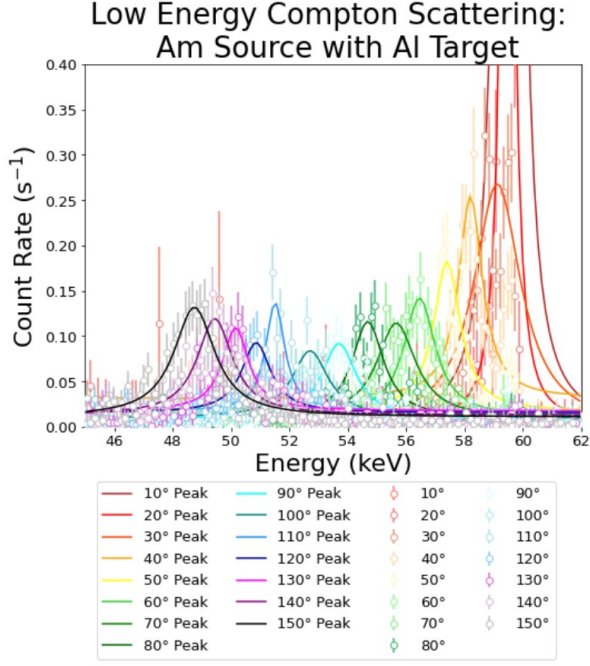


FIG. 6. The low energy Compton shift spectra with an aluminum target.

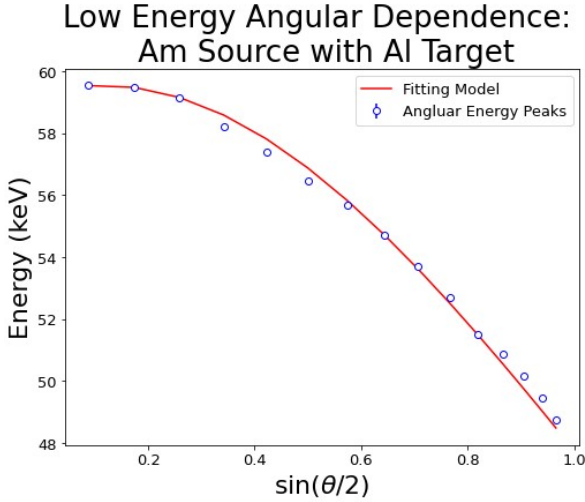


FIG. 7. The low energy Compton shift effect for an aluminum target plotted as the energy shift as a function of $\sin(\theta/2)$, where θ is the scattering angle.

The low energy Compton spectrum with an aluminum target is given in Fig. 6. Again, all inelastic peaks are less than the elastic one. The curve fitting for the relation between the scattering angle and the peak energy is $E' = 1/(a + b \sin^2 \frac{\theta}{2} + c \sin \frac{\theta}{2})$, with

$$\begin{aligned} a &= 0.016860 \pm 3.5536 \times 10^{-9} \\ b &= 0.021059 \pm 7.5075 \times 10^{-7} \\ c &= -0.002338 \pm 1.1152 \times 10^{-7} \end{aligned} \quad (18)$$

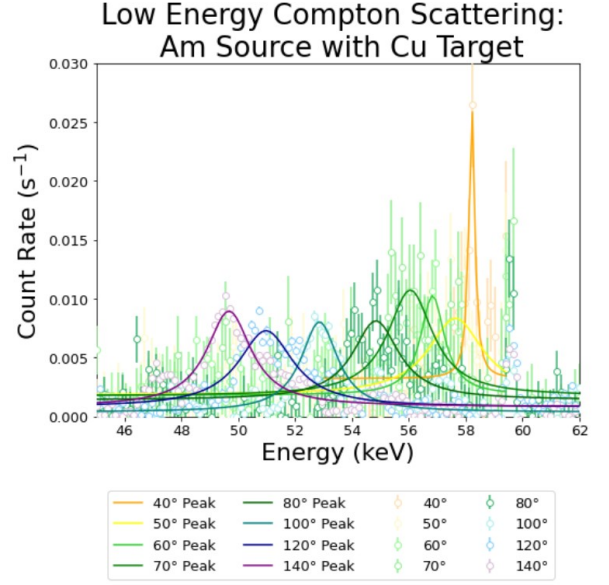


FIG. 8. The low energy Compton shift spectra with a copper target.

where a is in good agreement with Eq. (13), but b is a little bit off. Moreover, c gives the z -component of the electron momentum, as we will explain in the electron momentum distribution function. This curve fitting is explicitly shown in Fig. 7.

For copper, we performed the same analysis, and the energy spectrum and angular dependencies are given in Fig. 8 and Fig. 9 respectively. The corresponding fitting parameters for the copper target are:

$$\begin{aligned} a &= 0.017288 \pm 0.000173 \\ b &= 0.022852 \pm 0.003486 \\ c &= -0.00456 \pm 0.001602 \end{aligned} \quad (19)$$

For this fitting, our value for a is reasonably close to the accepted value, and again, b is off by about the same factor as the aluminum target fitting. Again, the c value gives us information on the z -component of the electron momentum.

In Fig. 10, we present the $\theta = 90^\circ$ electron momentum distribution function, where the dominant contribution comes from the $x = 0.097 \pm 0.011$ Lorentzian peak. In other words, lots of the outgoing electrons carry a small (about 9.7%) fraction of the source energy and most of the energy goes with the outgoing photons. If we zoom in to the low energy fraction region, we observe similar behaviors for another scattering angle (see Fig. 11). To leading approximation, if we only consider the peaks in the EDF distribution, the relation between the peak and the scattering angle is simply from the Compton shift in Fig. 6 and 7, so we omit the figure for it. However, the full EDF is a universal function for other scattering processes inside the Al material, like Comptonization simulation involving multiple Compton scattering.

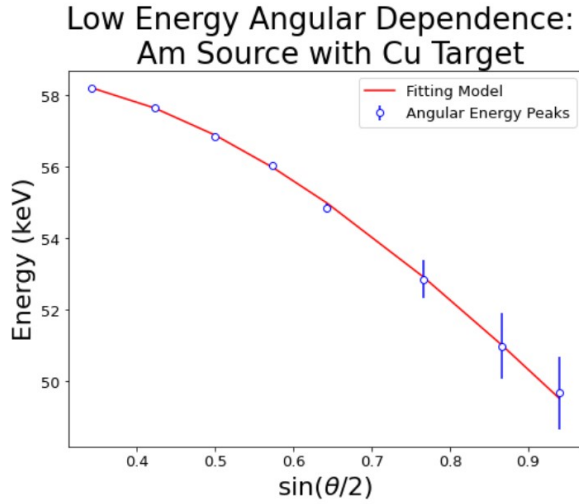


FIG. 9. The low energy Compton shift effect for a copper target plotted as the energy shift as a function of $\sin(\theta/2)$, where θ is the scattering angle.

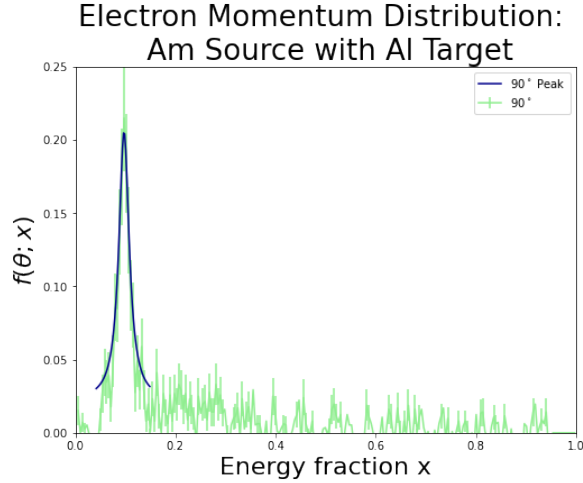


FIG. 10. Electron momentum distribution function for aluminum target at $\theta = 90^\circ$. We perform the fitting for the peak, which corresponds to the dominant electron energy fraction. The error is estimated by Poisson distribution.

Finally, we present the results of low energy scattering from a fixed angle off of different targets. At the fixed scattering angle of 80° , the elements had noticeably different peak distributions as seen in Fig. 12. While all energy peaks occurred at the same position, at about 54.5 keV, the widths of these peaks increased with increasing atomic mass of the scattering target. This relation is shown in Table I. Unfortunately, the data for lead was not taken for long enough to get a satisfactory peak above the background. So we had to throw out the data for lead because we could not fit a Lorentzian peak to the spectrum near an energy value of 54.5 keV. We were able to fit a Lorentzian peak to the silver tar-

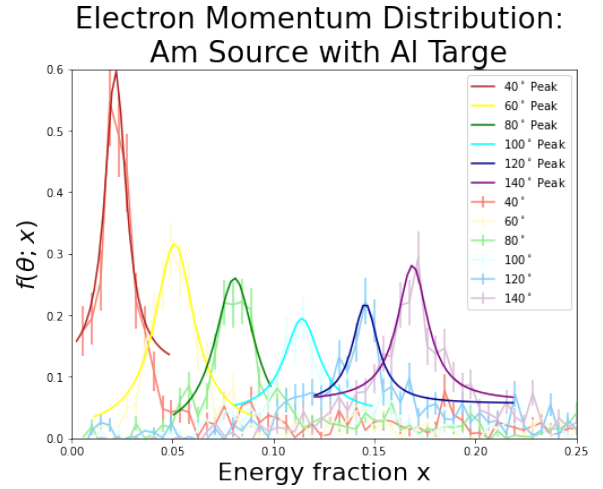


FIG. 11. Electron momentum distribution function for aluminum target at different scattering angles. Again the error is estimated by Poisson distribution.

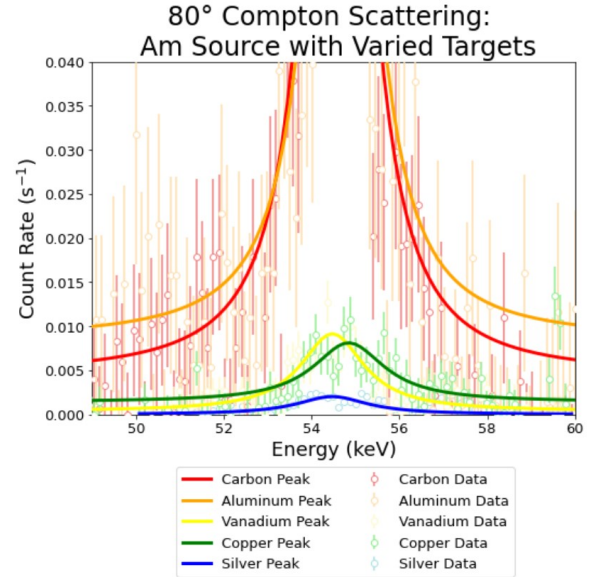


FIG. 12. The 80° low energy Compton shift spectra of various target elements.

get data, however the detector ran out of liquid nitrogen in the middle of data collection. This tripped the bias shutdown flooding our dataset with a lot of noise. This resulted in the recorded peak for the silver target being contaminated and making its result unreliable. This can clearly be seen in the massive error bars associated with the silver data. With the caveat of the unreliable silver data, the results displayed in the table make it clear that the spread of the peaks increase with atomic mass. We do not feel that we collected enough data to confidently fit this data with a function to predict the spread of the energy peaks for any scattering target based on its atomic mass. However, it is certainly something that could be

Scattering Target	Atomic Mass	Peak Position (keV)	Half-Width (keV)
Carbon	12.011	54.58 ± 0.0007	0.6570 ± 0.0015
Aluminum	26.982	54.67 ± 0.0007	0.6713 ± 0.0015
Vanadium	50.942	54.47 ± 0.1021	0.8823 ± 0.1864
Copper	63.546	54.84 ± 0.1363	0.9915 ± 0.2464
Silver	107.868	54.47 ± 6.6689	0.9851 ± 13.3435

TABLE I. The half-widths of the Lorentzian peaks determined by the fixed scattering angle of 80° . Atomic masses determined using the periodic table [16].

examined further with the testing of more elements as scattering targets.

III. CONCLUSION

In this experiment, we performed the Compton spectrum measurement for different sources and targets. Using the sodium-iodide scintillation detector, we measured the high energy Compton scattering of the cesium-137 source off of an aluminum target and calculated both the energy of the outgoing photons and the cross sections for different scattering angles. We found the energy shift was in complete agreement with the theoretical prediction in Eq. (7). Specifically, the values for $a = 1/E$ were very precise, which was convincing as we needed to

use the precise value of E for the calibration of the detectors. However, the differential cross section $\frac{1}{\sigma_1} \frac{d\sigma}{d\cos\theta}$ only agrees with the Klein-Nishina formula in Eq. (2) up to an unknown geometry factor Ω . Regarding the low energy spectra, we changed the source to americium-241 and measured the scattering by both an aluminum and copper target using the germanium detector. We found that the energy shifts are in good agreement with the next-to-leading order correction in Eq. (5). At the same time, we extracted the electron momentum distribution function $f(\theta; x)$ for aluminum from the Compton spectrum, which allows the calculation of other scattering processes in aluminum material. Finally, we also measured the Compton spectrum for different targets with a fixed scattering angle and found that the half-width grows as the atomic mass increases.

IV. ACKNOWLEDGEMENTS

We thank Joe Peidle and Jieping Fang for teaching us how to use the equipment and design the experiment

for Compton scattering. We appreciate Matteo Mitrano for lots of help on data analysis. Moreover we thank Jenny Hoffman for enlightening discussions and useful suggestions on the manuscript.

-
- [1] J. J. Thomson, *Conduction of electricity through gases* (University press, 1906).
 - [2] S.-y. Chen, A. Maksimchuk, and D. Umstadter, Experimental observation of relativistic nonlinear thomson scattering, *Nature* **396**, 653 (1998).
 - [3] A. H. Compton, A quantum theory of the scattering of x-rays by light elements, *Phys. Rev.* **21**, 483 (1923).
 - [4] Y. Rephaeli, Comptonization of the cosmic microwave background: The sunyaev-zeldovich effect, *Annual Review of Astronomy and Astrophysics* **33**, 541 (1995).
 - [5] W. Gordon, Der Comptoneffekt nach der Schrödingerschen Theorie, *Zeitschrift für Physik* **40**, 117 (1926).
 - [6] P. A. M. Dirac, Relativity quantum mechanics with an application to compton scattering, *Proceedings of the Royal Society of London. Series A, Containing papers of a mathematical and physical character* **111**, 405 (1926).
 - [7] P. A. M. Dirac *et al.*, *The principles of quantum mechanics*, 27 (Oxford university press, 1981).
 - [8] O. Klein and Y. Nishina, Über die streuung von strahlung durch freie elektronen nach der neuen relativistischen quantendynamik von dirac, *Zeitschrift für Physik* **52**, 853 (1929).
 - [9] L. M. Brown and R. P. Feynman, Radiative corrections to compton scattering, *Phys. Rev.* **85**, 231 (1952).
 - [10] R. N. Lee, M. D. Schwartz, and X. Zhang, Compton scattering total cross section at next-to-leading order, *Phys. Rev. Lett.* **126**, 211801 (2021).
 - [11] M. J. Cooper, Compton scattering and electron momentum determination, *Reports on Progress in Physics* **48**, 415 (1985).
 - [12] M. D. Schwartz, *Quantum Field Theory and the Standard Model* (Cambridge University Press, 2013).
 - [13] N. Johnson, S. Kotz, and N. Balakrishnan, *Continuous Univariate Distributions*, Continuous Univariate Distributions No. v. 2 (Wiley & Sons, 1994).
 - [14] W. Feller, V. Feller, and K. M. R. Collection, *An Introduction to Probability Theory and Its Applications*, An Introduction to Probability Theory and Its Applications

- No. v. 1-2 (Wiley, 1957).
- [15] R. B. Firestone and C. M. Baglin, *Table of isotopes*, 8th ed. (Wiley, New York, 1998).
- [16] W. M. Haynes, D. R. Lide, and T. J. Bruno, *CRC handbook of chemistry and physics* (CRC press, 2016).

APPENDIX

1. Calibrations of The Sodium-Iodide Detector

In this subsection, we perform the calibration of the sodium-iodide scintillation detector. First, we measured the energy spectra of americium-241, barium-133, sodium-22 and cesium-137 over 180 seconds and normalized for the count rate per second. We also recorded a background level, but it was so low with respect to the calibration data that we deemed it was insignificant to determine the position of the peaks (it was less than 1% of the signal around the peaks). We then fit the data with a Lorentzian distribution function [13, 14]:

$$f(x) = A \cdot \frac{\gamma^2}{(x - x_0)^2 + \gamma^2}. \quad (20)$$

For our purposes, the relevant parameter was the peak position, determined by x_0 in the equation above. The calibration spectra are shown in Fig. 13.

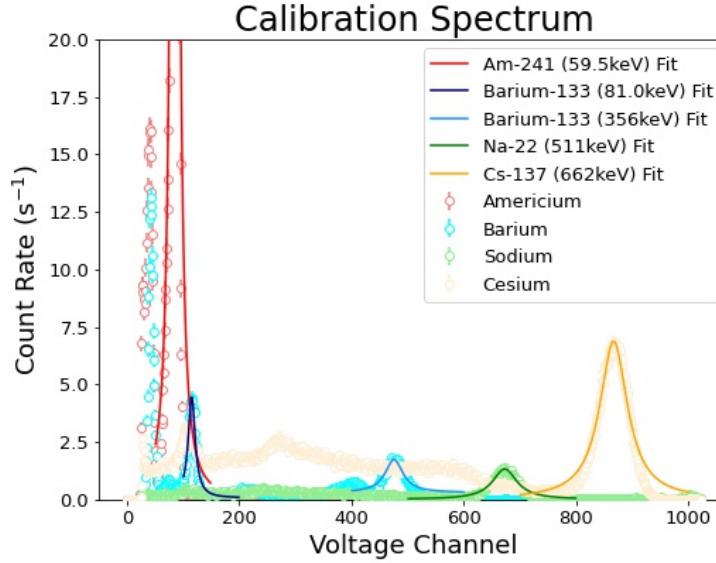


FIG. 13. The energy spectra for all the high energy calibration samples as measured by the sodium-iodide detector.

Calibration Sample	Peak Position (keV)
Americium-241	59.5
Barium-133	81.0
	356.0
Sodium-22	511
Cesium-137	662

TABLE II. The literature values of the peak positions [15] for the high energy calibration samples.

Each peak from the calibration spectra has an associated energy value as shown in Table II. Therefore, we have a relationship between the voltage channel and energy value of each calibration peak. We obtain the following linear model to assign each voltage channel, V , some associated energy value, E , in keV:

$$V = (1.2965 \pm 0.0007)E + (8.4085 \pm 0.0428) \quad (21)$$

This relation is shown in Fig. 14 and can be used to determine the energy value of each voltage channel. We estimated the error of the data with Poisson distribution and propagated it to the linear fitting.

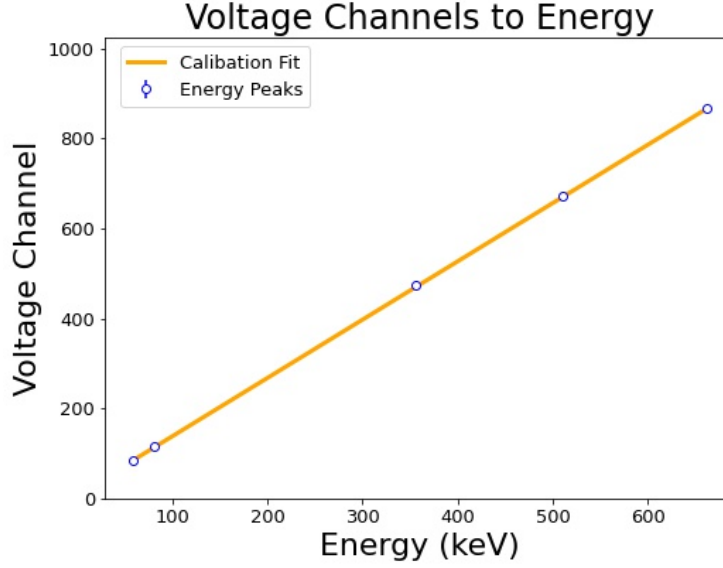


FIG. 14. The result of the high energy calibration for the sodium-iodide detector.

2. Calibrations of The Germanium Detector

The calibration of the Germanium detector is very similar to that of the sodium-iodide detector. For this calibration we used americium-241, cobalt-57 and uranium-238 as our calibration samples. Note that by alpha decay, we will also obtain energy spectra for neptunium-237, the daughter product of americium-241. Also, due to the long half-life of uranium-238, we will not see a spectrum for this isotope, but we will see its alpha decay daughter product, thorium-234. Again, we measured their energy spectra for 180 seconds and normalized for count rate per second. With another negligible background, we can fit these peaks with a Lorentzian model to find the peak positions. This plot is shown in Fig. 15.

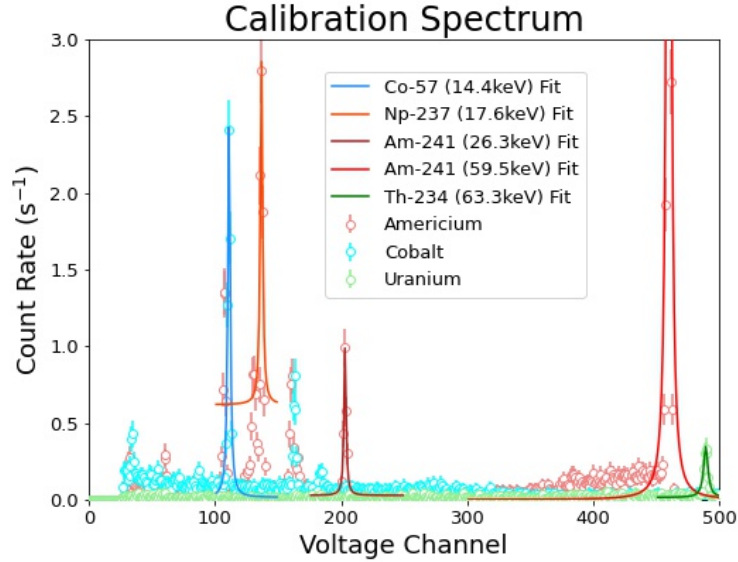


FIG. 15. The energy spectra for all the low energy calibration samples as measured by the germanium detector.

Calibration Sample	Peak Position (keV)
Americium-241	26.3
	59.5
Cobalt-57	14.4
Neptunium-237	17.6
Thorium-234	63.3

TABLE III. The literature values of the peak positions [15] for the low energy spectra calibration samples.

Each peak from the calibration spectra has an associated energy value as shown in Table III. Therefore, we have a relationship between the voltage channel and energy value of each calibration peak. We obtain the following linear model to assign each voltage channel, V , some associated energy value, E , in keV:

$$V = (7.6973 \pm 0.0008)E + (1.1304 \pm 0.0460) \quad (22)$$

This relation is shown in Fig. 16 and can be used to determine the energy value of each voltage channel. We estimated the error of the data with Poisson distribution and propagated it to the linear fitting.

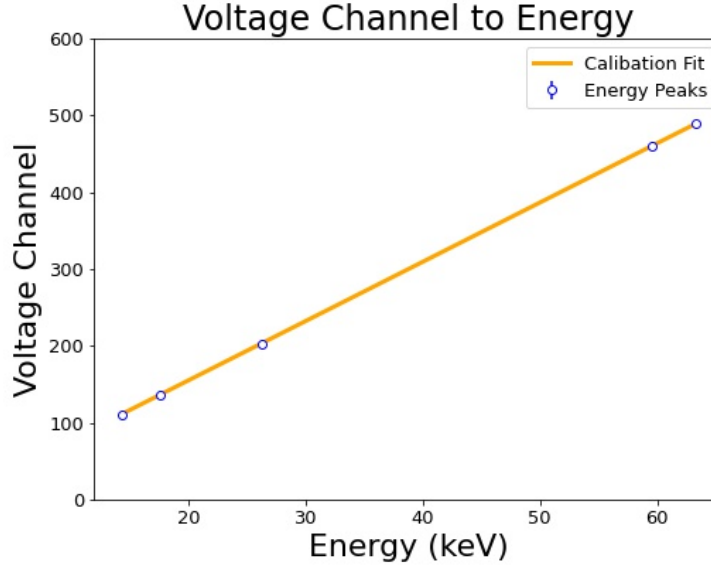


FIG. 16. The result of the low energy calibration for the germanium detector.

Since the voltage values of the Germanium detector change slightly when the apparatus is restarted, we redo this calibration procedure and obtain a new (albeit very similar) relation for Eq. (22) after each time we turn the power on and off.

3. Background Measurement for Compton Scattering

In order to correctly fit the energy spectra peaks at different angles, we had to first remove the background from our measurements. For every angle measurement, we also recorded an identical background sample, with the radiation sample still present, just with the scattering target removed. However, there was no straightforward way to complete this background removal. The background was a much too complicated distribution to fit with any reasonable function. Therefore, we decided to subtract a ‘smoothed’ background from each of our data samples. For each angle’s background we applied the `scipy.savgol.filter` function in python to smooth the data. We programmed this function to replace each data point with the average value of the five data points above and below that value. An example of the background data smoothing can be seen in Fig. 17. This ‘smoothed’ background can then be subtracted from the raw data for each corresponding measurement.

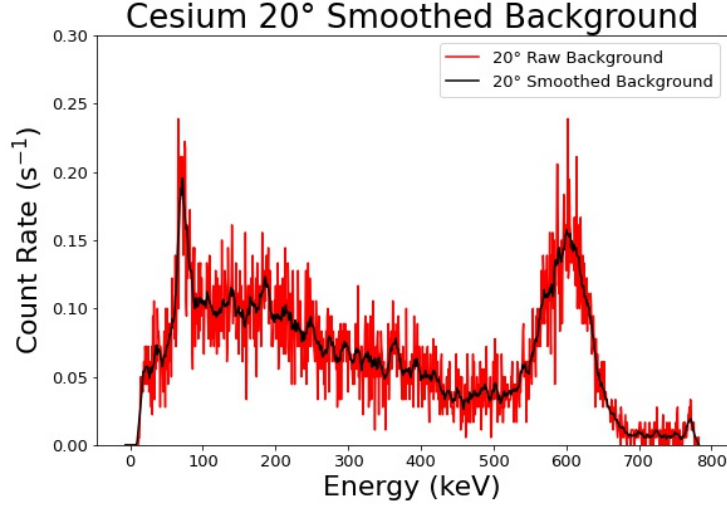


FIG. 17. An example of a smoothed background with respect to its raw data counterpart. The averaging across 11 points significantly reduces the random noise in the data.

4. The Width of The Lead Shield

In the high energy Compton scattering experiment, we used lead shields to restrict the area of the sodium-iodide detector so that we could detect the photons within a very small solid angle range. In Sec. IIC, in particular, Eq. (17), we find that there is a constant factor Ω that affects the cross section. This Ω is related to the width the lead shield.

To study how the width of the lead shield affects the experiment, we measured the energy spectra at the scattering angle $\theta = 90^\circ$ with different widths $d = 1$ cm, 2 cm, 3 cm and 4 cm. The results for the measurements are shown in Fig. 18, where we subtract the smoothed background and perform the Lorentzian peak fitting. The spectra were very similar once the backgrounds were removed. For our experiment, we decided to use a 3cm gap width in the lead shield.

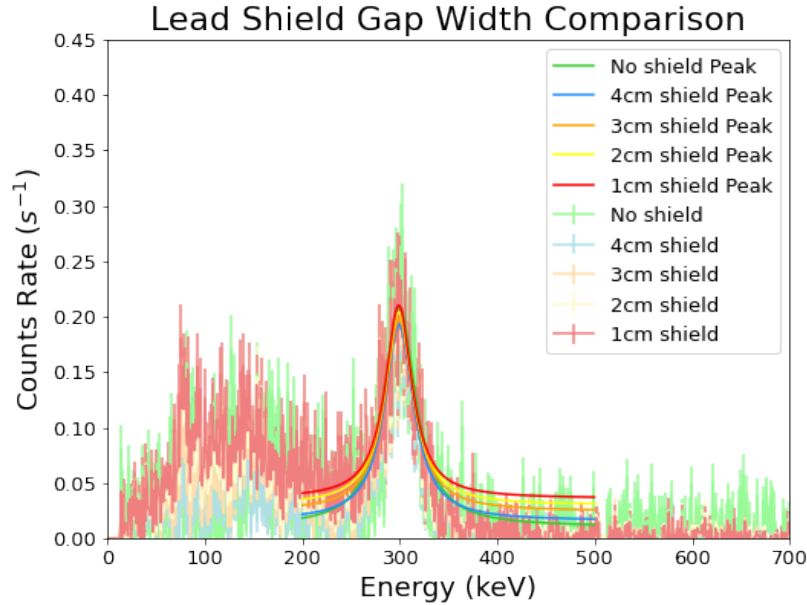


FIG. 18. The energy spectra at scattering angle $\theta = 90^\circ$ with different widths of the lead shield gap.